



# Influence of applied in-plane strain on transverse thermal conductivity of 0°/90° and plain weave ceramic matrix composites

Daxu Zhang<sup>1</sup>, D.R. Hayhurst<sup>\*</sup>

School of Mechanical, Aerospace and Civil Engineering, George Begg Building C.004, The University of Manchester, Sackville Street, Manchester, M13 9PL, UK

## ARTICLE INFO

### Article history:

Received 4 August 2010

Received in revised form 15 November 2010

Available online 1 December 2010

### Keywords:

Ceramic matrix composites

Tows

Unit cell

0–90 uni-directional and woven composites

Thermal conductivity degradation

Orthotropic material

## ABSTRACT

A computationally economic finite-element-based stress analysis model, developed previously by the authors, has been extended to predict the thermal behaviour of ceramic matrix composites with strain-induced damage. The finite element analysis utilises a solid element to represent a homogenised orthotropic medium of a heterogeneous uni-directional tow. The non-linear multi-axial strain dependent thermal behaviour has been discretised by multi-linear curves, which have been implemented by a user defined subroutine, USDFLD, in the commercial finite element package, ABAQUS. The model has been used to study the performance of two CMC composites: a SiC (Nicalon) fibre-calcium aluminosilicate (CAS) matrix, 0°/90° cross-ply laminate Nicalon-CAS; and, carbon fibre-dual carbon-SiC matrix (C/C-SiC), plain weave laminate DLR-XT. The global through-thickness thermal conductivity degradation with composite uni-axial strain has been predicted. Comparisons have been made between the predictions and experimental data for both materials, and good agreement has been achieved. For the Nicalon-CAS 0°/90° cross-ply the dominant mechanism of thermal conductivity degradation is combined fibre failure and associated wake debonding; and, for the DLR-XT plain weave the same mechanisms act in combination with out-of-plane shear failure.

© 2010 Elsevier Ltd. All rights reserved.

## 1. Introduction

The superior material properties of ceramic matrix composites (CMCs), e.g. low density and good mechanical and thermal properties at high temperatures, make them favourable materials for use in: rocket nozzles; thermal protection systems; and gas turbine engines (Marshall and Cox, 2008). Increased operating temperatures from 900–1200 °C for coated metallic superalloys, to above 1300 °C, for CMCs, have the potential to achieve higher thermal efficiencies and lower emissions (Evans and Naslain, 1995). The economic use of CMCs in engineering components and structures, in such demanding environments at these temperatures, requires an ability to simulate the material, and the component response at both the design and manufacturing stages (McGlockton et al., 2003). To perform optimal design of these engineering components, a highly efficient yet accurate computational model is a necessary requirement, due to the complex spatial topology and interactive damage mechanisms of woven CMCs.

The very strong coupling between mechanical behaviour and thermal properties (Sheikh et al., 2009) is, at the present time, not well understood, and is not capable of being accurately pre-

dicted. Hence, the driver for this research is the need to describe and predict these effects at the design stage. Some of the first approaches to thermal finite-element modelling were two dimensional (Lu and Hutchinson, 1996; Klett et al., 1999). The limitation of their approaches is simplicity, which does not reflect the complexities of real composites. Sheikh et al. (2001) have presented a complex weave model of a plain weave CMC. Their model is three-dimensional, and is a step towards the modelling of complex composite architectures. Their research included the effect of directionality in thermal transport by the introduction of the individual properties of fibre and matrix. However, the main deficiency was the absence of initial porosity. This level of understanding was further advanced by Del Puglia et al. (2004a,b, 2005) for the same (DLR-XT) material, by inclusion of porosity at the macro-unit cell level.

An earlier paper, Zhang and Hayhurst (2010), studied the mechanical behaviour of two CMCs, a Nicalon-CAS 0°/90° laminate and a DLR-XT plain weave composite. A very good prediction of experimental stress-strain data was made from tow properties using the tow model of Tang et al. (2009). This paper addresses the influence of applied in-plane uni-axial straining on the through-thickness thermal conductivity. This objective has been achieved by the further development of the finite element models of Zhang and Hayhurst (2010). The fidelity of the models is judged by comparison with experimental thermal conductivity data of Sheikh et al. (2009).

<sup>\*</sup> Corresponding author. Tel.: +44 161 306 3818; fax: +44 161 200 4166.

E-mail address: [d.r.hayhurst@manchester.ac.uk](mailto:d.r.hayhurst@manchester.ac.uk) (D.R. Hayhurst).

<sup>1</sup> Present address: School of Naval Architecture, Ocean and Civil Engineering, Shanghai Jiao Tong University, 800 Dongchuan Road, Shanghai 200240, China.

Two classes of fibres and associated matrices are considered here. They are (a) Nicalon-CAS material (Tang and Hayhurst, in press) and (b) C/C-SiC DLR-XT material (Tang et al., in press). Both materials have been studied experimentally by Sheikh et al. (2009). The former material is a cross-ply laminate consisting of calcium aluminosilicate (CAS) glass ceramic matrix reinforced with SiC (Nicalon) fibres (Harris et al., 1992). The layout is  $(0^\circ/90^\circ)_5$ , where the subscript, 5 signifies 5 groups of  $0^\circ/90^\circ$  plies, equivalent to 10 laminae, with loose plain woven fabric skins. The latter, which is used as a fabrication aid, contributes little to the thermo-mechanical properties and has been neglected. The DLR-XT material is a 10 high laminae plain weave carbon fibre/amorphous carbon matrix-SiC matrix composite. Idealised unit cells of the two materials are shown schematically in Fig. 1.

## 2. Thermal behaviour of a uni-directional CMC tow

As outlined in the introduction, finite element analysis will be carried out using tow stress-strain and thermal conductivity-strain behaviour.

### 2.1. Tow longitudinal thermal conductivity

Tang et al. (2009) have postulated that longitudinal thermal conductivity is controlled by the air gaps introduced on matrix cracking, with regular crack separation distance  $w$ , and fibre failure, c.f. Fig. A1 of the Appendix. They have derived equations, based on the thermo-mechanical properties of the constituent materials, which can be numerically integrated to produce variations of the local tow longitudinal thermal conductivity,  $k_{Long}^\ell$ , with local tow strain,  $\varepsilon_{33}^\ell$ . For convenience, the derivations of Tang et al. (2009) have been summarised in Sections A1.1 and A1.2 of the Appendix for the mechanical and thermal behaviour, respectively. The relevant equations for variation of  $k_{Long}^\ell/k_{Long}^{\ell-Initial}$  with the tow damage variable  $\omega$  are given by Eqs. (A6) and (A7), and for the variation of  $k_{Long}^\ell/k_{Long}^{\ell-Initial}$  with  $\varepsilon_{33}^\ell$  are given by coupled numerical integration of Eqs. (A2) and (A4). Using these relations, and values of  $k_{Long}^{Initial}$ , the variation of  $k_{Long}^\ell$  with  $\varepsilon_{33}^\ell$  has been obtained from the material parameters of the composite base materials. These are given in Figs. 2(a) and 3(a) for Nicalon-CAS and DLR-XT, respectively.

For Nicalon-CAS an initial value of  $k_{Long}^{Initial} = k_{33}^\ell = 1.530 \text{ Wm}^{-1} \text{ K}^{-1}$  has been determined from Eq. (A5), using the constituent materials data given in Tables 1 and 2 of Tang and Hayhurst (in press); and has been used to determine the curve of Fig. 2(a). For the DLR-XT material an initial value of  $k_{Long}^{Initial} = k_{33}^\ell = 20.38 \text{ Wm}^{-1} \text{ K}^{-1}$  has been determined from Eq. (A5), using the constituent materials data given in Tables (A1) and (A2) of Tang et al. (in press); and has been used to determine the curve of Fig. 3(a). Both Figs. 2a and 3a have been discretised as multi-linear curves using typically 25 data points.

Here the strain tensor is defined in local tow coordinates, where 3 is the direction parallel to the fibres, 2 is the direction orthogonal

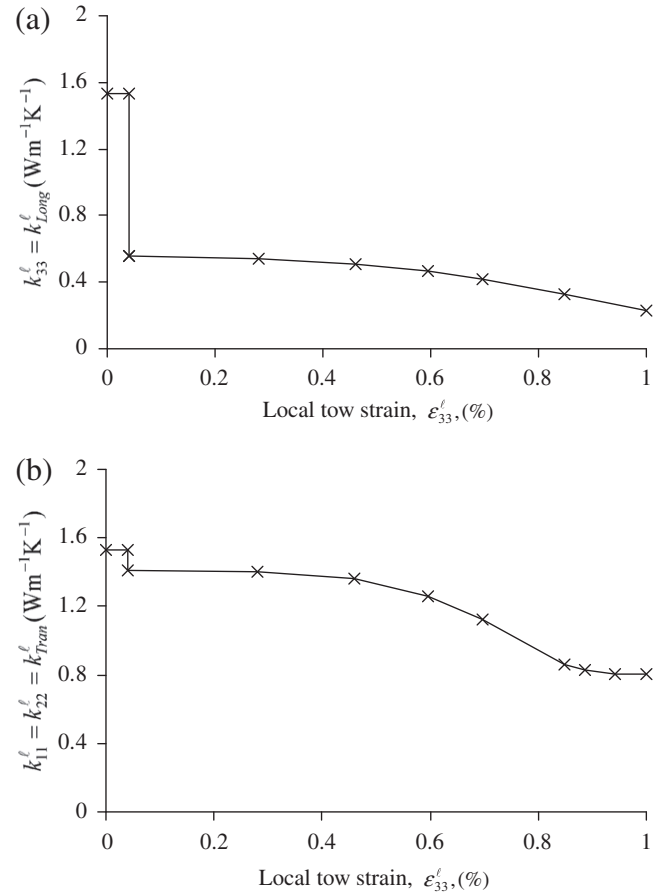


Fig. 2. Thermal material properties of a uni-directional Nicalon-CAS tow (a) multi-linear longitudinal thermal conductivity-strain curve; and (b) multi-linear transverse thermal conductivity-strain curve.

to the fibres and out of the laminate surface, and 1 is the direction orthogonal to the fibres and coincident with the laminate plane. The first step reduction in  $k_{Long}^\ell$  shown in Figs. 2(a) and 3(a) is due to matrix cracking and the subsequent monotonic decrease that results from fibre failure. The data in Figs. 2(a) and 3(a) is used as the discretised multi-linear materials input data for the finite element model.

### 2.2. Tow transverse thermal conductivity

Tang et al. (2009) have shown that the degradation of transverse thermal conductivity is controlled by the process of wake debonding which produces a cylindrical air gap at the interface between fibre and matrix in a block of material associated with a single fibre located between two adjacent matrix as shown in

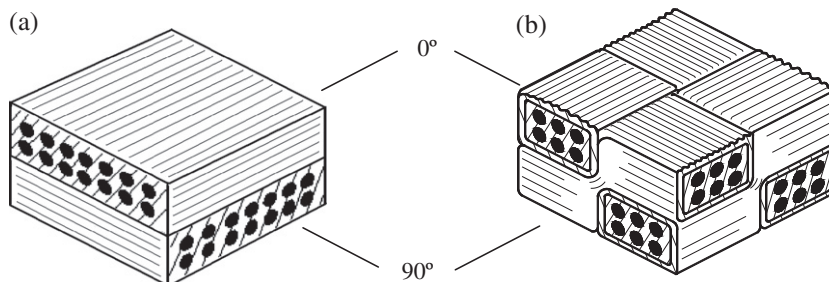
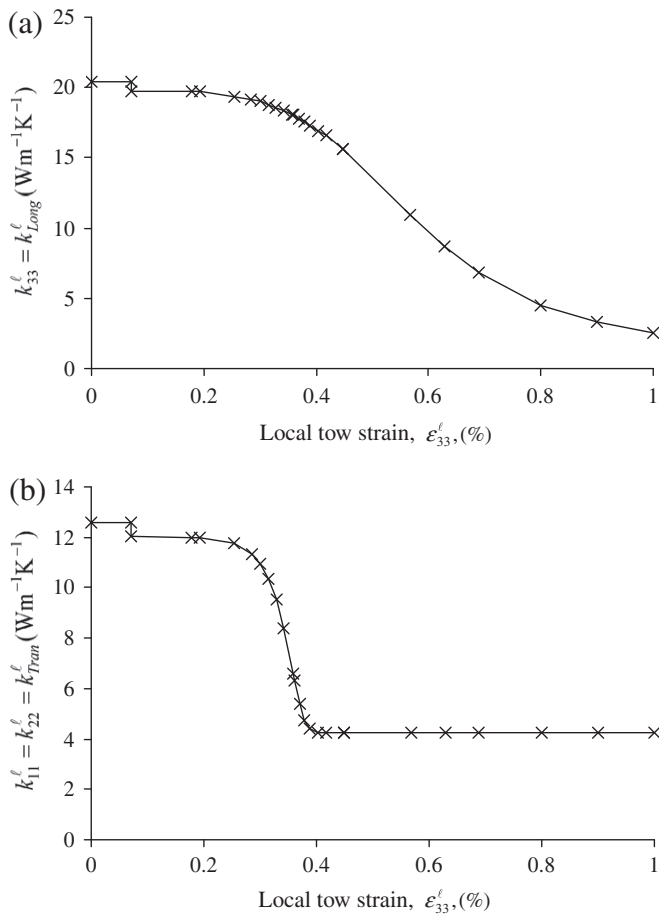
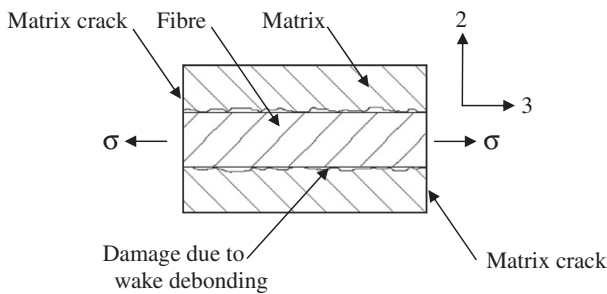


Fig. 1. Schematic drawings of unit cells of: (a)  $0^\circ/90^\circ$  Nicalon-CAS, and (b) plain weave DLR-XT.



**Fig. 3.** Thermal material properties of a uni-directional DLR-XT tow (a) longitudinal thermal conductivity-strain curve; and (b) transverse thermal conductivity-strain curve.



**Fig. 4.** Schematic diagram of a section of a fibre-matrix block of length  $w$  extracted from between adjacent matrix cracks. The interface is shown with (a) damage as a result of wake debonding; and (b) further interfacial damage due to transverse loading.

Fig. 4, and in Fig. 11 of Blacklock and Hayhurst (in press). The poor transverse thermal conductivity of the cylindrical air gap prevents transverse heat flow {2-direction} through the fibre and some of the matrix. The degradation of the local transverse thermal conductivity,  $k_{Tran}^l$ , with local tow strain,  $\epsilon_{33}^l$ , is related to the ratio,  $N/N_T$ , where  $N$  is the number of failed blocks and  $N_T$  is the total number of blocks in a tow segment, as shown schematically in Fig. A1. The variation of  $k_{Tran}^l/k_{Tran}^{l-Initial}$  with  $\epsilon_{33}^l$  has been determined for the Nicalon-CAS material using Eq. (A15) and for the DLR-XT material using Eq. (A16). The initial transverse thermal conductivity of the tow  $k_{Tran}^{l-Initial}$  for both materials has been calculated using Eq. (A9). For Nicalon-CAS an initial value of  $k_{Tran}^{l-Initial} = k_{11}^l = k_{22}^l =$

$1.530 \text{ Wm}^{-1} \text{ K}^{-1}$  has been obtained using data from Table 2 of Tang and Hayhurst (in press); N.B. the fact that  $k_{Long}^{l-Initial}$  and  $k_{Tran}^{l-Initial}$  have same numerical initial values is fortuitous and a consequence of the relatively high value of the thermal conductivity of the aluminosilicate matrix. For DLR-XT an initial value of  $k_{Tran}^{l-Initial} = k_{11}^l = k_{22}^l = 12.56 \text{ Wm}^{-1} \text{ K}^{-1}$ , has been obtained using data from Tables A1 and A2 of Tang et al. (in press). The graphs of  $k_{Tran}^l$  against  $\epsilon_{33}^l$  for Nicalon-CAS and DLR-XT are given in Figs. 2(b) and 3(b), which again are used as the multi-linear input data using typically 25 data points for the finite element model. For both graphs given in Figs. 2(b) and 3(b) the mechanism of transverse tow thermal degradation is combined wake debonding and fibre failure as modelled by Tang et al. (2009).

### 2.3. Effects of shear strain on the longitudinal and through-thickness thermal conductivity

In  $0^\circ/90^\circ$  composites, Fig. 1(a), the fibres/tows are straight and little shear strain is induced by in-plane composite remote stress  $\sigma_\infty$  and constituent materials property mismatch. However, in woven composites, Fig. 1(b), the situation is different as shown schematically in Fig. 5. Fig. 5(a) shows the weave segment in the circled region, which in turn is shown in Fig. 5(b) with stress and strain components defined in the local coordinate system, where  $\sigma_\infty$  and  $\epsilon_\infty$  are the global remote stress and strain, respectively. The figure schematically shows failure of the fibre/matrix interface due to local shear and normal stress. When the shear strain,  $\epsilon_{32}^l$ , is greater than the critical failure strain,  $\epsilon_{32}^{ls}$ , then the continuity of the fibre-matrix interface is broken and partial failure is assumed to have occurred. The partial failure affects the mechanical behaviour, but the thermal response is unchanged since the failure surfaces are in contact. If the normal stress,  $\sigma_{22}^l$ , is less than a small positive lower level,  $\sigma_{22}^{ll}$ , i.e.  $\sigma_{22}^l < \sigma_{22}^{ll}$ , the fibres and matrix are assumed to be in sufficient contact for heat transfer to take place. However, when  $\sigma_{22}^l > \sigma_{22}^{ll}$ , an air gap is assumed to form, and transverse heat transfer is prevented.

The effects of longitudinal through-thickness shear failure condition,  $\epsilon_{32}^l > \epsilon_{32}^{ls}$ , and  $\sigma_{22}^l > \sigma_{22}^{ll}$  on transverse conductivity are

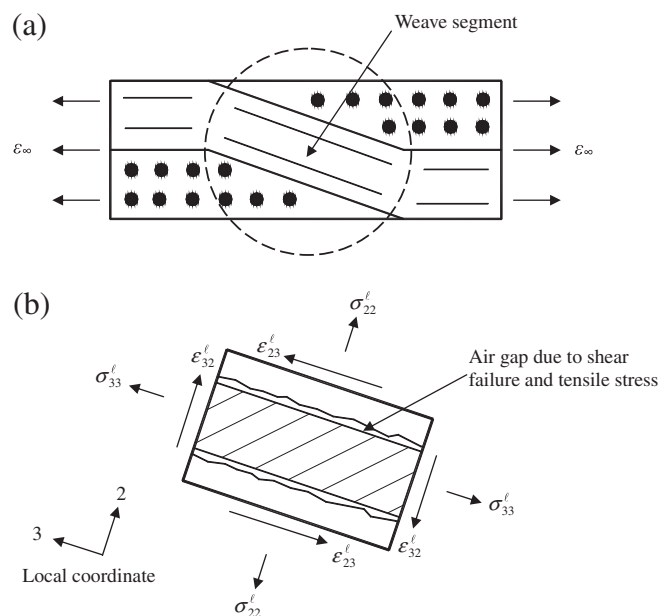


**Fig. 5.** Schematic showing (a) a woven unit cell under longitudinal straining; and (b) fibre/matrix element within the circled weave segment showing interface damage as a result of shear failure and tensile stress.

assumed to dominate over the effects of wake debonding that results in the separation of the two surfaces on the failure plane due to  $\sigma_{33}^{\ell}$ . Hence in the studies carried out here, one of the two following mechanisms will be considered:

- (i) Wake debonding alone driven by longitudinal tension  $\sigma_{33}^{\ell}$ ; or
- (ii) shear failure induced by shear or transverse tension,  $\sigma_{32}^{\ell} > \sigma_{32}^s$ , with  $\sigma_{22}^{\ell} > \sigma_{22}^s$ .

### 3. Formulation of the finite element model

This paper reports the development of a coupled thermal-stress finite element model that has been based on the stress-displacement model of Zhang and Hayhurst (2010). In this previous work, a uni-directional tow (or an assemblage of tows to form a lamina) was chosen to be the basic constituent in the finite element model, and therefore an entire tow or a lamina, which consists of thousands of fibres embedded in matrix, was represented by a single 8-node solid finite element (Fig. 6). The material properties were assumed to be multi-linear elastic and the discretised non-linear stress-strain and Poisson's ratios-strain curves are used, c.f. Figs. 10 and 14 of Zhang and Hayhurst (2010). The finite element package ABAQUS (SIMULIA, 2006) with a user-defined subroutine UMAT was used to carry out the simulations; its operation will be outlined in a later section. This method has the benefit of being able to model a tow by a single finite element with orthotropic properties. The coupled thermal-stress model reported here has been formulated using strain dependent thermal material properties. The details of the formulation for mechanical behaviour can be found in Zhang and Hayhurst (2010). The formulation of the thermal behaviour of the model is addressed as follows:

#### 3.1. Heat flow in a homogenised uni-directional tow

A heterogeneous uni-directional tow or lamina was homogenised to a single block shown in Fig. 6, which has the same overall dimensions and equivalent orthotropic thermal material properties as the actual material. For the present three dimensional steady-state heat conduction problem, there are three independent tow thermal conductivities:  $k_1$ ,  $k_2$ , and  $k_3$ , defined relative to the local tow axes given in Fig. 6.

For anisotropic continua the steady-state heat conduction equation is given by Fourier's law (Fourier, 1822), which has been particularised for composite materials by White and Knutsson (1982) and Argyris et al. (1995):

$$\begin{Bmatrix} q_1 \\ q_2 \\ q_3 \end{Bmatrix} = - \begin{bmatrix} k_{11} & k_{12} & k_{13} \\ k_{21} & k_{22} & k_{23} \\ k_{31} & k_{32} & k_{33} \end{bmatrix} \begin{Bmatrix} \partial T / \partial x_1 \\ \partial T / \partial x_2 \\ \partial T / \partial x_3 \end{Bmatrix}, \quad (1)$$

where  $q_i$  is the heat flux;  $k_{ij}$  is the thermal conductivity; and  $\partial T / \partial x_i$  is the thermal gradient ( $i, j = 1, 2, 3$ ). Classical thermodynamic argu-

ments have shown that the conductivity tensor  $k_{ij}$  is symmetric with  $k_{ij} = k_{ji}$ ; and for an orthotropic material, the coupling terms in the thermal conductivities matrix  $k_{ij}$  are zero, and therefore Eq. (1) becomes:

$$\begin{Bmatrix} q_1 \\ q_2 \\ q_3 \end{Bmatrix} = - \begin{bmatrix} k_{11}^{\ell} & 0 & 0 \\ 0 & k_{22}^{\ell} & 0 \\ 0 & 0 & k_{33}^{\ell} \end{bmatrix} \begin{Bmatrix} \partial T / \partial x_1 \\ \partial T / \partial x_2 \\ \partial T / \partial x_3 \end{Bmatrix}. \quad (2)$$

For the local coordinates, c.f. Fig. 5(b), used in this study,  $k_{33}^{\ell}$  is the thermal conductivity along the tow,  $k_{22}^{\ell}$  is the out-of-plane (through-thickness) transverse tow thermal conductivity, and  $k_{11}^{\ell}$  is the in-plane transverse tow conductivity.

#### 3.2. Determination of unit cell heat flux

To perform a finite element analysis at the composite unit cell level, c.f. Nicalon-CAS unit cell in Fig. 7, the tow non-linear thermal conductivities were discretised as the multi-linear curves given in Figs. 2 and 3 for Nicalon-CAS and DLR-XT, respectively. The mechanical straining in the 3-direction was imposed in terms of the displacement boundary conditions as a succession of small strain increments; and over each strain increment the combined mechanical-thermal problem was solved for a unity thermal gradient between the upper and lower surfaces of the unit cell. For each strain increment, element thermal conductivities were evaluated by ABAQUS from Figs. 2 and 3 using the mechanical strain fields at the start of the increment; and these values were used by ABAQUS to compute the values of heat flux (Watts  $m^{-2}$ ) at nodes over the unit cell lower face, at the end of the current strain increment. These local values were integrated over the lower surface to determine the total heat flux. The values of the latter are numerically equal to the transverse thermal conductivity of the unit cell, since a unity thermal gradient boundary condition was imposed. Such values of transverse thermal conductivity were determined at the end of each successive strain increment.

#### 3.3. Implementation of subroutine USDFLD in ABAQUS (SIMULIA, 2006)

The present thermo-mechanical model has been implemented using the finite element package, ABAQUS/standard and a user defined subroutine, USDFLD. The discretised strain dependent tow thermal conductivities, c.f. Figs. 2 and 3, have been defined as functions of the strain field variables in the input file. For each increment, the subroutine USDFLD was used to read the local strains at each integration point and then to define the tow thermal conductivity properties using these strains. Automatic incrementation algorithms and the increment redefinition variable, PNEWDT, defined in ABAQUS, were continuously updated to ensure that values of the field variables at the end of the relevant strain increments were located exactly at the discretised points of Figs. 2 and 3.

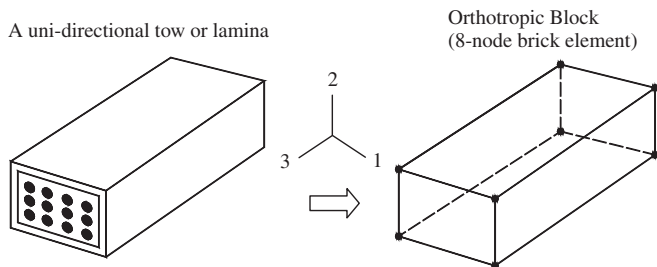


Fig. 6. Schematic representation of the homogenisation of a uni-directional tow or lamina to a single block of orthotropic material.

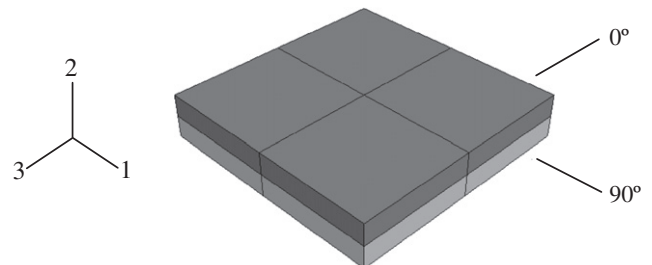


Fig. 7. Finite element mesh of the unit cell of a  $(0^\circ/90^\circ)_5$  Nicalon-CAS laminate.



### 3.4. Numerical convergence studies

In the user subroutine USDFLD the material properties were calculated using the strain values at the start of an increment, which then remain unchanged throughout that increment. This may introduce a small error dependent upon on the rate of change of material properties with strain, and on the magnitude of the strain increment. To reduce this error to acceptable levels and achieve the required solution convergence, the increment size was maintained at less than a set value of 0.01. The latter value was established by carrying out repeated runs until the values of the composite global thermal conductivities were repeatable to be within 0.1%.

## 4. Thermal conductivity-strain response of 0°/90° Nicalon/CAS laminates

In this section, the thermal conductivity-strain response of a 0°/90° Nicalon-CAS laminate, c.f. Fig. 1(a), under uni-axial straining along the 0° fibres was predicted using the finite element approach described in the previous section. The effects of fibre waviness on the overall out-of-plane thermal conductivity of the laminate were also modelled. The material properties of a uni-directional Nicalon/CAS lamina, defined in Section 4.3, were used as input data to predict the global thermal behaviour of the laminate; and finally, a comparison was made between predictions and experimental data.

### 4.1. Boundary condition

A unit cell of the (0°/90°)<sub>5</sub> Nicalon/CAS laminate, was used that consists of four 0° ply and four 90° ply finite elements. The dimensions of the Nicalon-CAS unit cell are  $2.5 \times 2.5 \times 0.4616 \text{ mm}^3$  and its mesh is shown in Fig. 7. A total of eight finite elements were used to allow modelling of fibre waviness. The square dimension  $2.5 \times 2.5 \text{ mm}^2$  has arbitrarily been taken as the same as that for the DLR-XT unit cell studied by Tang et al. (in press); and the thickness of 0.4616 mm has been taken from Sheikh et al. (2009). Displacement boundary conditions were applied to the unit cell to simulate uni-axial straining along the 0° fibre direction (direction 3 in Fig. 7). Steady state heat conduction was modelled by application of a unity thermal gradient between the top and bottom faces of the unit cell, and all the other faces were lagged.

### 4.2. Modelling of waviness

During manufacture of the ceramic matrix composites, some degree of waviness in the alignment of the fibres or tows is introduced. This has been measured from the micrographs presented by Sheikh et al. (2009). The resulting models are exactly the same as those used by Zhang and Hayhurst (2010) and a waviness or misalignment angle of  $\xi = 7^\circ$  has been used, as shown in Fig. 10 of their paper; and, the reader is referred to Section 4.1 for full details.

### 4.3. Nicalon-CAS material properties

This section addresses the specification of both mechanical and thermal material data.

#### 4.3.1. Nicalon-CAS: Tow mechanical properties

Exactly the same material property data are described in Section 4.2 of Zhang and Hayhurst (2010). They have been calculated by numerical integration of Eqs. (A2) and (A4) using the materials data given in Table 1 of Tang and Hayhurst (in press). The variation of five properties with local strain,  $\epsilon_{ij}^L$  ( $i, j = 2-3$ ), are given. These are: longitudinal tow stress,  $\sigma_{33}^L$ ; tow Poisson's ratios,  $\nu_{31}^L$  and  $\nu_{32}^L$ ; transverse tow stresses,  $\sigma_{22}^L$ ; and tow shear stresses,  $\sigma_{23}^L$ . The

variation of these parameters, with  $\epsilon_{33}^L$ ,  $\epsilon_{22}^L$  and  $\epsilon_{23}^L$ , are provided in multi-linear discretised form, c.f. Fig. 10 of Zhang and Hayhurst (2010).

#### 4.3.2. Nicalon-CAS: Longitudinal tow thermal properties

Equations for the derivation of these properties are given in the Section A1.2 (i) of the Appendix; and the calculated numerical values are given in Section 2.1 and shown in Fig. 2(a).

#### 4.3.3. Nicalon-CAS: Transverse tow thermal properties

Equations for the derivation of these properties are given in the Section A1.2 (ii) of the Appendix; and the calculated numerical values are given in Section 2.2 and shown in Fig. 2(b).

### 4.4. Predictions for Nicalon-CAS 0°/90° unit cell

#### 4.4.1. Composite mechanical response

The predicted variation of the applied global stress  $(\sigma_{33})_\infty$  with  $(\epsilon_{33})_\infty$  for the Nicalon-CAS has been presented by Zhang and Hayhurst (2010), and for convenience is reproduced in Fig. 8. Two predicted curves are shown: one for zero tow waviness,  $\xi = 0^\circ$ , and the other for a waviness of  $\xi = \pm 7^\circ$ . The curve for  $\xi = \pm 7^\circ$  falls mid-way between the two experimental curves.

#### 4.4.2. Composite thermal response

For the materials tested by Sheikh et al. (2009), no results were obtained for global in-plane composite thermal conductivity. For this reason, no attempt has been made to predict in-plane thermal conductivities.

Predictions of the variations of out-of-plane thermal conductivity,  $k_{22}$ , with composite strain,  $(\epsilon_{33})_\infty$ , are given in Figs. 9 and 10 for zero waviness,  $\xi = 0^\circ$ , and a waviness angle of  $\xi = \pm 7^\circ$ , respectively. For both Figs. 9 and 10, two experimental data curves show an acceptable level of scatter. However, examination of the  $(\sigma_{33})_\infty - (\epsilon_{33})_\infty$  curve of Fig. 8 for experimental data 1 shows a non-monotonic trend. This feature is reflected in the  $k_{22} - (\epsilon_{33})_\infty$  curve of Figs. 9 and 10. Since the reasons for this are unclear, greater credence will be given to experimental data set 2. Since the Nicalon-CAS composite is 0°/90°, and hence avoids the weave section shown in Fig. 5(b), the shear interface failure mode described in Section 2.3 has not been triggered in the data of Fig. 9, for  $\xi = 0^\circ$ , and also in Fig. 10, for  $\xi = \pm 7^\circ$ , since the values of  $\sigma_{32}^L$  are very low. In comparing experimental data and model predictions, it is important to recognise that the predictions are for a single unit cell. In the experiments, the test piece contained many hundreds of unit cells. Therefore the predicted distinct drop in  $k_{22}$  at matrix cracking,  $(\epsilon_{33})_\infty = 0.04\%$ ,

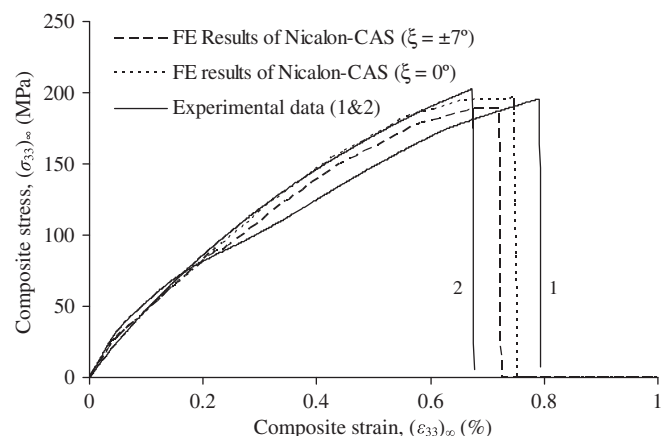


Fig. 8. Comparison of predicted and experimental stress-strain curves for Nicalon-CAS.

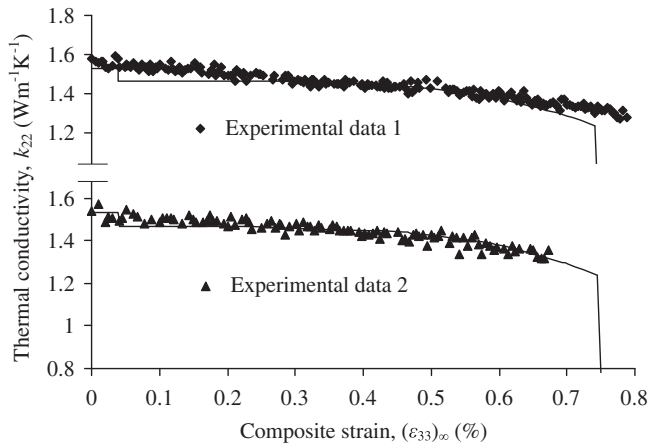


Fig. 9. Predicted through-thickness thermal conductivities for Nicalon-CAS ( $\xi = 0^\circ$ ).

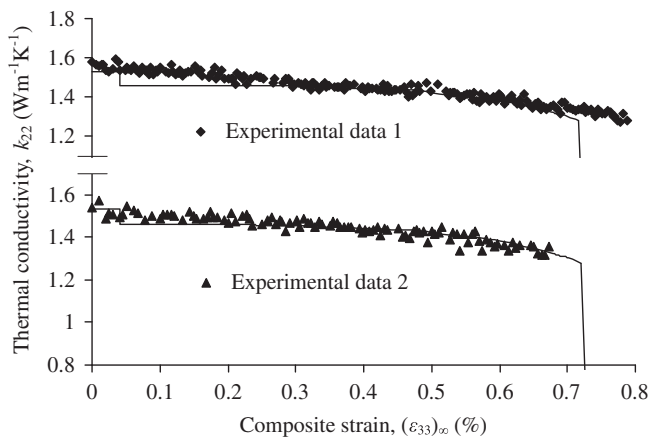


Fig. 10. Predicted through-thickness thermal conductivities for Nicalon/CAS ( $\xi = \pm 7^\circ$ ).

would not be expected to be observed in the experimental data. Instead a statistical average would be anticipated over a finite strain range. Bearing this in mind the predictions agree well with experimental results over the entire strain range. The effect of waviness in changing from  $\xi = 0^\circ$  to  $\xi = \pm 7^\circ$  is slight with the  $\xi = \pm 7^\circ$  curve being moved slightly upwards. In an overall sense the best prediction is for a waviness of  $\xi = \pm 7^\circ$ .

## 5. Thermal conductivity-strain response of plane weave DLR-XT composites

In this section, predictions of thermal conductivity-strain response are reported for a plain weave DLR-XT composite, c.f. Fig. 1(b), under uni-axial straining along the  $0^\circ$  tows. Effects of the tow waviness on the overall stress-strain curve of the composite are modelled. The mechanical and thermal material properties of a uni-directional DLR-XT tow are used as input data to predict the overall mechanical and thermal behaviour of the composite; and finally, a comparison is made between predictions and experimental data.

### 5.1. Formulation of the finite element model

A methodology similar to that developed for the Nicalon/CAS material was employed to create the unit cell model of a plain weave DLR-XT composite. The only difference between the two

models was the mesh and geometry, because the topology of the DLR-XT composite is much more complex due to the woven tows.

One important objective of this study is to develop an approach which is capable of analysing large scale composites. This makes it difficult to create a finite element model, which captures woven features of a tow yet uses a minimum number of finite elements. The mesh and geometry of the DLR-XT unit cell model, shown in Figs. 11 and 12, are believed to be one of the optimal solutions. The mesh for a single tow, consists of 12 elements: two 8-node brick elements, six 6-node wedge elements, and four 4-node tetrahedral elements c.f. Fig. 11(a). The DLR-XT unit cell model is an assembly of four tow models, which are bonded together through the fully contacted interfaces c.f. Fig. 11(b). The finite element dimensions are given in Fig. 12 together with the weave angle,  $\zeta = 9.1^\circ$ , and waviness angle  $\xi = \pm 7^\circ$ . The tow/fibre directions shown in Fig. 12 for the four 4-noded tetrahedral elements that connect to the centre line of the unit cell, orthogonal to the upper face, are inclined at approximately  $45^\circ$  to the edge of the unit cell. At first sight this appears to be a severe assumption, but it is a consequence of using the minimum number of elements to model the unit cell. Increasing the number of elements would permit a more faithful representation of the fibre/tow flow.

Inevitably, modelling the unit cell with the twelve elements shown in Fig. 11 will result in some loss of accuracy; however, subsequent comparison of predicted and experimental results shows this to be acceptable. However, it is these features that make possible the finite element analysis of large components. Yang and Cox (2003) concluded that strains averaged over a gauge volume whose linear dimensions are equal to or exceed half the cross-sectional dimensions of a tow, are reasonably mesh independent. For the present DLR-XT unit cell model, the majority of the elements (83.4% by volume) are approximately equal to this gauge volume; and, in addition their strain distributions are rather uniform. Hence, it is reasonable to use the local strain at an integration point to predict different failure modes of the material. The fidelity of the model was assessed by comparison with experimental data in Section 5.4.

A periodic displacement boundary condition was applied to the unit cell to simulate a uni-axial strain along the  $0^\circ$  tow direction (direction 3 in Fig. 11). Steady state heat conduction was modelled by application of a unity thermal gradient between the top and bottom faces of the unit cell, and all the other faces were lagged.

### 5.2. Modelling of waviness

Waviness also exists in woven ceramic matrix composites, and is frequently more severe than that for conventional laminates. The waviness angle,  $\xi$ , in the DLR-XT material has been measured over a larger region than that shown in the micrograph of Sheikh et al. (2009) and a value of  $\xi = \pm 7^\circ$  has been obtained. The resulting models are exactly the same as those used by Zhang and Hayhurst (2010); and have a maximum fibre misalignment angle, i.e. sum of the weave and waviness angles, in some elements of  $\xi + \zeta = 16.1^\circ$ . The reader is referred to Section 5.2 of their paper for details.

### 5.3. Material properties

#### 5.3.1. DLR-XT: Tow mechanical properties

Exactly the same material property data has been used as that described in Section 5.3 of Zhang and Hayhurst (2010). They have been calculated by numerical integration of Eqs. (A2) and (A4) using the materials data given in Tables A1 and A2 of Tang et al. (in press). The variations of nine properties are given with local strain,  $\epsilon_{ij}^l$  ( $i, j = 1-3$ ). These are longitudinal tow stress,  $\sigma_{33}^l$ ; tow Poisson's ratios,  $\nu_{31}^l$ ,  $\nu_{32}^l$  and  $\nu_{12}^l$ ; transverse tow stresses,  $\sigma_{11}^l$  and

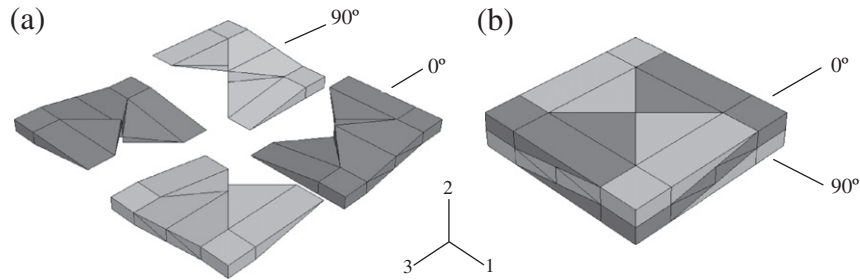


**Fig. 11.** Mesh and geometry of the unit cell model of a plain weave DLR-XT composite: (a) exploded view; and (b) assembled view. The 90° tows have light shading, and the 0° tows have dark shading.

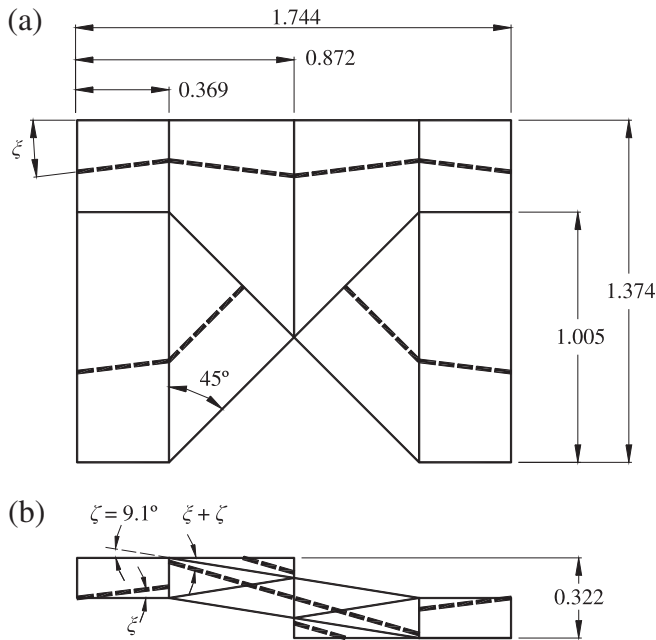


**Fig. 12.** Schematic diagram of the 0° tow, shown in the left-hand illustration of Fig. 11(a), showing dimensions of the finite element unit cell, and tow/fibre alignment within the elements: (a) plan view, and (b) side elevation. The broken lines denote tow alignment with weave angle  $\zeta = 9.1^\circ$  and waviness angle  $\xi = \pm 7^\circ$ . All linear dimensions are in mm.

$\sigma_{22}^t$ ; and tow shear stresses,  $\sigma_{12}^t$ ,  $\sigma_{13}^t$  and  $\sigma_{23}^t$ . The characteristics of these parameters, with  $\epsilon_{ij}^t$  ( $i, j = 1-3$ ), are provided in multi-linear discretised form, c.f. Fig. 15 of Zhang and Hayhurst (2010).

### 5.3.2. DLR-XT: Longitudinal tow thermal properties

Equations for the derivation of these properties are given in the Section A1.2 of the Appendix; and the calculated numerical values are given in Section 2.1, and shown in Fig. 3(a).

### 5.3.3. DLR-XT: Transverse tow thermal properties

Equations for the derivation of these properties are given in the Appendix A1.2 (ii) of the Appendix; and the calculated numerical values are given in Section 2.2, and shown in Fig. 3(b).

## 5.4. Predictions

### 5.4.1. Mechanical response

The predicted variation of composite stress,  $(\sigma_{33})_\infty$ , with composite strain,  $(\epsilon_{33})_\infty$  has been presented by Zhang and Hayhurst (2010) and for convenience is reproduced in Fig. 13. Two predicted curves are shown: one for zero waviness,  $\xi = 0^\circ$ , and the other for a

waviness of  $\xi = \pm 7^\circ$ . The curve for  $\xi = \pm 7^\circ$  is closest to the experimental data.

### 5.4.2. Thermal response

For the materials tested by Sheikh et al. (2009), no results were obtained for in-plane composite thermal conductivity. For this reason, no attempt has been made to predict in-plane thermal conductivities. Predictions of the variation of composite transverse thermal conductivity,  $k_{22}$ , with composite strain,  $(\epsilon_{33})_\infty$ , are given in Figs. 14 and 15 for  $\xi = 0^\circ$  and  $\xi = \pm 7^\circ$  without consideration of the effects of shear strain failure described in Section 2.3; and in Figs. 16 and 17 for  $\xi = 0^\circ$  and  $\xi = \pm 7^\circ$  with consideration of shear strain failure. For all the Figs. 14–17, the results of experiment 2 will be given a low priority due to the excessive scatter on the data. The reason for this scatter is unknown.

*Without shear failure:* In connection with Figs. 14 and 15 for predictions without consideration of the effects of shear failure, the curve for waviness of  $\xi = 0^\circ$  shown in Fig. 14 predicts the experimental data best. The curve for  $\xi = \pm 7^\circ$ , Fig. 14, starts to deviate from the experimental data at the strain  $(\epsilon_{33})_\infty \approx 0.19\%$ , and the error increases thereafter. Since the composite possesses waviness of  $\xi = \pm 7^\circ$ , the model for  $\xi = \pm 0^\circ$  is not appropriate.

*With shear failure:* When the effects of shear failure are considered the predictions of composite thermal conductivity-strain variations were obtained as shown in Figs. 15 and 16. The curve of Fig. 16 for  $\xi = 0^\circ$  predicts the experimental data extremely well. The shear failure mechanism, introduced in Section 2.3 is assumed to be triggered when the transverse stress exceeds a lower bound,  $\sigma_{22}^t > \sigma_{22}^{tL}$ . Since no data is available for  $\sigma_{22}^{tL}$ , it has been determined by best fitting to experimental data. A value of  $\sigma_{22}^{tL} = 3.5$  MPa has been determined. The curve that includes waviness  $\xi = \pm 7^\circ$  shown in Fig. 17 predicts the experimental data less well than for  $\xi = 0^\circ$ , but is nonetheless a good prediction.

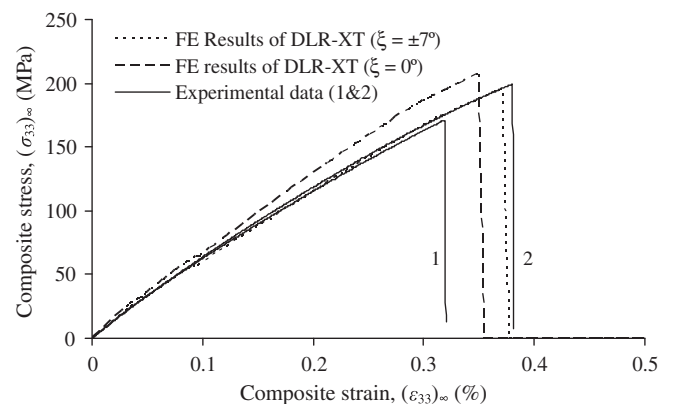


**Fig. 13.** Predicted stress-strain curve for DLR-XT.

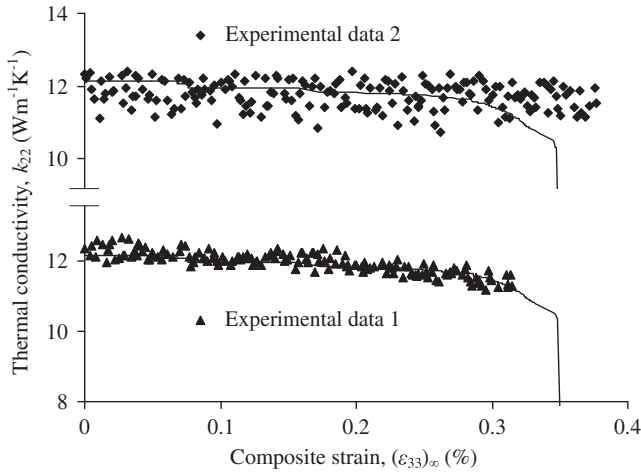


**Fig. 14.** Predicted through-thickness thermal conductivities for DLR-XT ( $\xi = 0^\circ$ ) with no effects of shear failure.

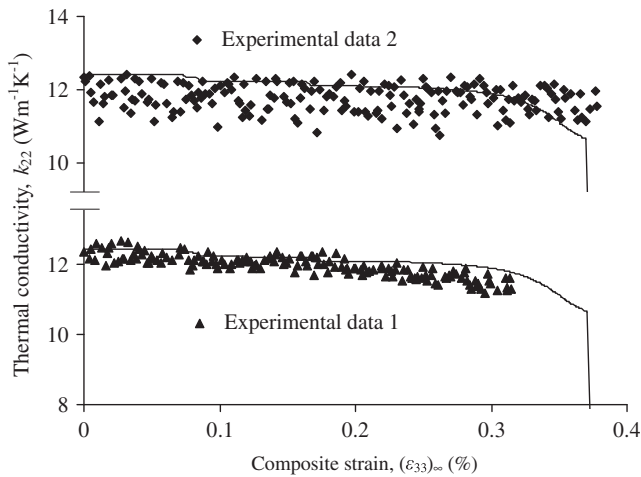


**Fig. 15.** Predicted through-thickness thermal conductivities for DLR-XT ( $\xi = \pm 7^\circ$ ) with no effects of shear failure.

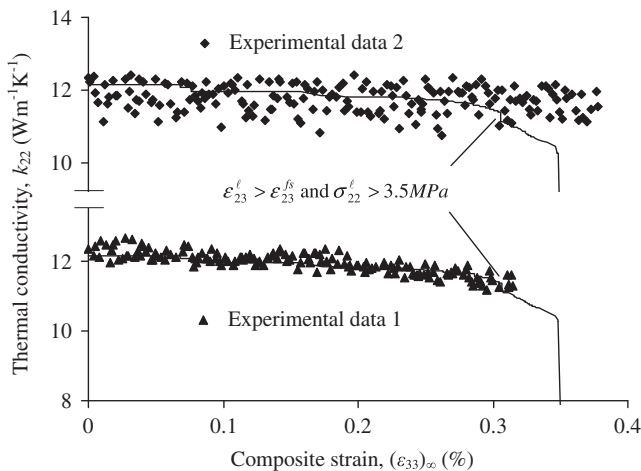


**Fig. 16.** Predicted through-thickness thermal conductivities for DLR-XT ( $\xi = 0^\circ$ ) with effects of shear failure when  $\epsilon_{23}^\ell > \epsilon_{23}^{fs}$  and  $\sigma_{22}^\ell > 3.5 \text{ MPa}$ .

Closer examination of the prediction in Fig. 17 shows a sharp drop in the curve at  $(\epsilon_{33})_\infty \approx 0.17\%$ . This is due to the shear failure mode being activated  $\epsilon_{23}^\ell > \epsilon_{23}^{fs} = 0.1152\%$  (c.f. Fig. 15(d) of Zhang and Hayhurst, 2010) and overriding the reduction in thermal

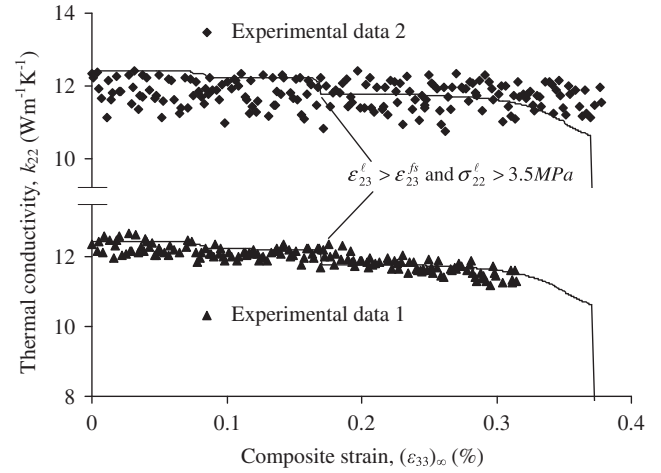


**Fig. 17.** Predicted through-thickness thermal conductivities for DLR-XT ( $\xi = \pm 7^\circ$ ) with effects of shear failure when  $\epsilon_{23}^\ell > \epsilon_{23}^{fs}$  and  $\sigma_{22}^\ell > 3.5 \text{ MPa}$ .

conductivity due to wake debonding, as introduced in Section 2.3. As expected this sharp drop is absent in Fig. 15, for which the waviness angle is  $\xi = \pm 7^\circ$  and shear effects are not included.

Since waviness is present in this material, the prediction shown in Fig. 17, which is significantly better than that shown in Fig. 15, best describes the true behaviour. Therefore the plain weave DLR-XT has its out-of-plane transverse thermal conductivity actively reduced by the shear failure mechanism coupled with a waviness angle of  $\xi = \pm 7^\circ$ .

#### 5.4.3. Composite Through-thickness heat flux for zero waviness $\xi = 0^\circ$

Predictions of composite through-thickness heat flux,  $\text{Wm}^{-2}$ , for an applied unity through-thickness thermal gradient,  $1^\circ \text{ km}^{-1}$ , are presented in Figs. 18 and 19 for zero tow waviness  $\xi = 0^\circ$ . The figures show only one pair of mating orthogonal tows, with the complementing pair having been removed for visual simplicity. For clarity, the flux fields are presented for tows with zero waviness, because the corresponding figure for non-zero waviness is made complex by sign changes in flux associated with the plus and minus values of  $\xi$ . The ABAQUS post processor only makes it possible to illustrate heat flux in the tow local coordinates, and each figure shows the flux normal to  $q_2^\ell$ , and parallel to  $q_3^\ell$ , the fibres.

Figs. 18 and 19 show heat flux in the  $0^\circ$  and the orthogonal degree  $90^\circ$  tows for  $q_2^\ell$  normal to, and  $q_3^\ell$  parallel to, the tows/fibres, respectively. Three levels of composite strain are addressed:  $(\epsilon_{33})_\infty = 0.3018\%$ ;  $(\epsilon_{33})_\infty = 0.316\%$ ; and  $(\epsilon_{33})_\infty = 0.353\%$ . The first two strain values straddle the strain at which out-of-plane shear failure takes place at  $(\epsilon_{33})_\infty = 0.306\%$ , c.f. Fig. 16 for  $\xi = 0^\circ$ , and the last value relates to unit cell/composite failure. Composite staining  $(\epsilon_{33})_\infty$  takes place parallel to the  $0^\circ$  and is orthogonal to the  $90^\circ$  tows. The flux field plots are now discussed for  $q_2^\ell$  normal to, and  $q_3^\ell$  parallel to, the tows/fibres.

##### 5.4.3.1. Flux normal to fibres/tows, $q_2^\ell$ – Fig. 18.

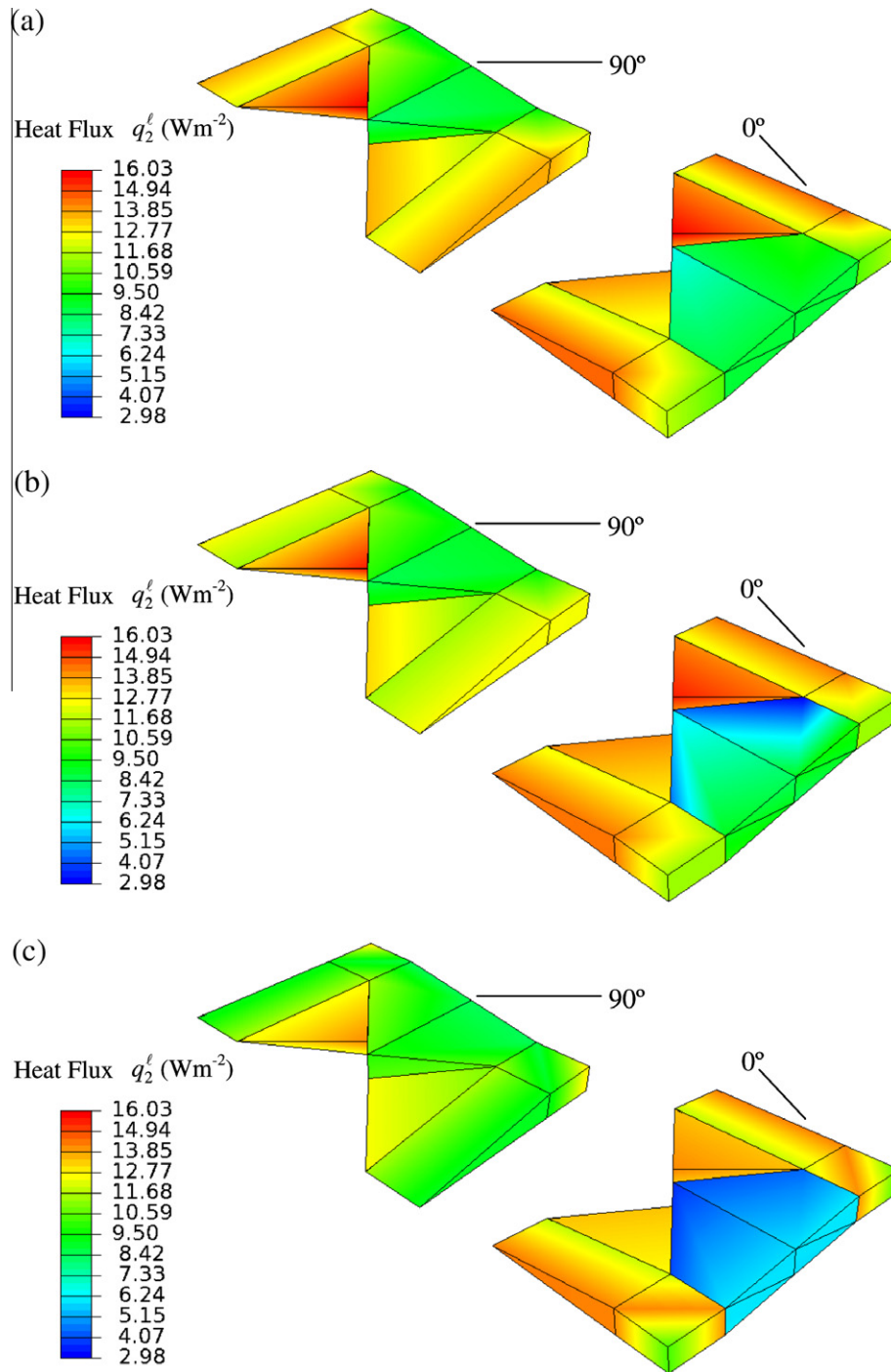
(a) Before out-of-plane shear failure  $(\epsilon_{33})_\infty = 0.3018\%$  – Fig. 18(a).

Fig. 18(a) shows that both the  $0^\circ$  and  $90^\circ$  tows have very similar flux fields. Those elements contained in the upper and lower surfaces have flux levels of  $q_2^\ell = 12.77\text{--}16.03 \text{ Wm}^{-2}$  compared with  $q_2^\ell = 8.5 \text{ Wm}^{-2}$  for the inclined elements with,  $\zeta = 9.1^\circ$ , for the woven tows.

(b) After out-of-plane shear failure  $(\epsilon_{33})_\infty = 0.3160\%$  – Fig. 18(b).

The flux levels in the  $0^\circ$  degree elements of the right-hand illustration of Fig. 18(b), contained in the upper and lower surfaces, are the same as those shown in Fig. 18(a). This is





**Fig. 18.** Heat flux normal to fibres,  $q_2^l$ , for zero tow waviness  $\xi = 0$ : (a) immediately before out-of-plane shear failure at  $(\epsilon_{33})_\infty = 0.3018\%$ ; (b) immediately after out-of-plane shear failure at  $(\epsilon_{33})_\infty = 0.3018\%$ ; and, (c) at partial unit cell/composite failure at  $(\epsilon_{33})_\infty = 0.3530\%$ .

due to the fibres being aligned in the 0 direction and to a negligible increase in the local strain  $(\epsilon_{33})_\infty$  in that direction. However, in the same right-hand illustration of Fig. 18(b), the flux levels  $q_2^l$  in the elements with inclined woven tows,  $\zeta = 9.1^\circ$ , are dramatically different than those given in Fig. 18(a). This is due to the out-of-plane shear failure being triggered in those elements, which causes the flux levels to fall from  $11.25 \text{ Wm}^{-2}$  given in Fig. 18(a), before shear failure to  $4.55 \text{ Wm}^{-2}$  afterwards.

The flux levels in the 90° elements of the left-hand illustration of Fig. 18(b), contained in the upper and lower surfaces, are less than those shown in Fig. 18(a). The latter is not due

to fibre failure, and the associated wake debonding, since the fibres are aligned orthogonal to the 0° direction of  $(\epsilon_{33})_\infty$  straining, and hence undergoes virtually no strain. Instead the lower flux level is due to the inclined elements located above and below, which undergo out-of-plane shear failure, the latter elements are not shown in this figure. These inclined elements, whose thermal conductivities are low, reduce the heat flow through the adjacent elements above and below.

(c) At partial unit cell/composite failure  $(\epsilon_{33})_\infty = 0.3530\%$  – Fig. 18(c). The left-hand illustration of Fig. 18(c), for the 90° tow, shows heat flux at cell/composite failure to be

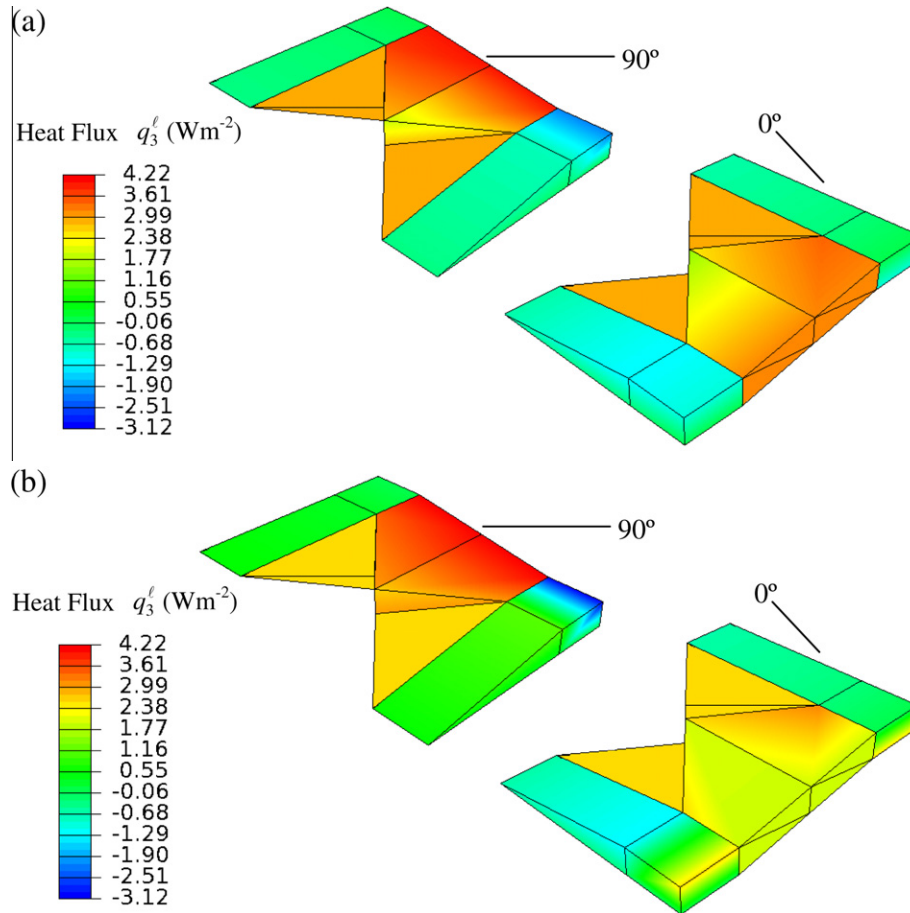


**Fig. 19.** Heat flux parallel to fibres,  $q_3^f$ , for zero tow waviness  $\zeta = 0$ : (a) immediately before out-of-plane shear failure at  $(\varepsilon_{33})_\infty = 0.3018\%$ ; and, (b) at unit cell/composite failure at  $(\varepsilon_{33})_\infty = 0.3530\%$ .

relatively uniform at  $q_2^f = 10.45 \text{ Wm}^{-2}$ . This value has changed slightly from that shown in Fig. 18(a) and (b); with the change being due to the inclined elements, located above and below, which undergo out-of-plane shear failure. In contrast, the right-hand illustration of Fig. 18(c), for the  $0^\circ$  tow, shows a more widespread reduction in flux due both to out-of-plane shear failure and to fibre failure and wake debonding due to  $(\varepsilon_{33})_\infty$  straining.

**5.4.3.2. Flux,  $q_3^f$ , parallel to fibres/tows – Fig. 19.** In Fig. 19 only two flux plots are presented for conditions before out-of-plane shear failure  $(\varepsilon_{33})_\infty = 0.3018\%$ , Fig. 19(a); and, at partial unit cell/composite failure  $(\varepsilon_{33})_\infty = 0.3530\%$ , Fig. 19(b). Flux field plots for the situation after out-of-plane shear failure at  $(\varepsilon_{33})_\infty = 0.3160\%$  have not been presented since they are almost identical to those shown in Fig. 19(a). The small negative values of heat flux shown in Fig. 19 are a consequence of the finite element approximations associated with the relatively large elements employed.

(a) Before out-of-plane shear failure  $(\varepsilon_{33})_\infty = 0.3018\%$  – Fig. 19(a). Both the left and right-hand figures of Fig. 19(a) are relatively similar. The major difference is in the inclined,  $\zeta = 9.1^\circ$ , woven tow elements. The right-hand  $0^\circ$  tow, being aligned with the  $(\varepsilon_{33})_\infty$  straining direction has undergone thermal conductivity degradation due only to fibre failure, since wake debonding does not influence longitudinal heat flux.

(b) At partial unit cell/composite failure  $(\varepsilon_{33})_\infty = 0.3530\%$  – Fig. 19(b). The heat flux shown in the left-hand  $90^\circ$  tow of Fig. 19(b) is almost the same as that shown in Fig. 19(a).

However, the right-hand  $0^\circ$  tow, being aligned with the  $(\varepsilon_{33})_\infty$  straining direction has undergone thermal conductivity degradation due only to fibre failure, since out-of plane shear failure and wake debonding do not influence longitudinal heat flux.

**5.4.3.3. Mechanism of transverse unit cell heat flux.** Heat flux normal to the fibres  $q_2^f$  is the dominant mode of transverse, through-thickness, heat flux, and is assisted to some degree by the component of heat flux parallel to the fibres/tows.

The heat flux  $q_3^f$  parallel to the fibres tends to follow a pattern provided that a failure mechanism does not intervene; the flow is from the upper surface along the fibres, if they are inclined relative to the direction of the thermal gradient, at a higher rate, down the tows inclined at  $\zeta = 9.1^\circ$ , to the lower unit cell surface. This is aided by the superior longitudinal thermal conductivity of the fibres. Hence, when all four tows are assembled there are four downward parallel paths along which heat can flow; this takes place simultaneously with the heat flux normal to the fibres.

## 6. Discussion of results

The results of the paper are now discussed under the following headings: mechanical response, thermal response and heat flux:

### 6.1. Mechanical response

For Nicalon CAS two levels of waviness have been considered  $\zeta = 0^\circ$  and  $7^\circ$  and the effect of increased waviness on the composite

stress–strain curve is to increase flexibility i.e. larger strains for the same stress, and to reduce failure strains.

For the DLR-XT material the same two levels of waviness have been considered  $\xi = 0^\circ$  and  $7^\circ$ , and the effect of increased waviness is to increase flexibility and increase failure strains. The latter effect on failure strains is unexpected, but it is believed to be due to stress redistribution between parallel load paths of adjacent tows. In this way, when the weakest tows reach the local failure criterion local unloading take place and the stronger tows continue to load. By this mechanism, larger failure strains are achieved. Since Nicalon-CAS has no weave this mechanism does not operate and reduced failure strains are produced.

## 6.2. Thermal response

For the two levels of waviness considered for the Nicalon CAS material little difference is predicted in the transverse thermal conductivity-composite uni-axial strain curves. However the prediction for a waviness angle of  $\xi = 7^\circ$  is marginally better.

As cited in Section 2.2, and by Tang et al. (2009), the physical mechanism responsible for thermal property degradation is wake debonding; and, as one would expect for a  $0^\circ/90^\circ$  composite the mechanism of out-of-plane shear failure is not triggered.

For the DLR-XT material the predictions for  $0^\circ$  of waviness, and without out-of-plane shear failure, are good; however, the micrographs of Sheikh et al. (2009) clearly show the presence of waviness and this possibility has to be excluded. On inclusion of failure due to out-of-plane shear very good predictions of the composite transverse thermal conductivity-strain curve have been achieved for both  $\xi = 0^\circ$  and  $7^\circ$ . However, the theory has to be accepted that includes waviness; and hence thermal conductivity degradation takes place by out-of-plane shear and by wake debonding that accompanies fibre failure. Another possible mechanism of transverse thermal conductivity degradation is inter laminae cracking/failure; however, this mode of failure is not expected since the composite processing route ensures that the inter laminae zone has the properties of the matrix. For that reason, this failure mechanism is not anticipated and it has been neglected.

## 6.3. Heat flux

For both materials it is evident that when the thermal gradients are applied orthogonal to the fibre/tow axis it is difficult for heat to flow along the fibres. However, when fibre inclination due to the weave angle is introduced, then a component of heat flow along the fibres can be achieved. Under these circumstances, the often superior longitudinal thermal conductivity can sometimes be exploited. This effect is minimal with the  $0/90$  lay-up of the Nicalon-CAS material; but, it is possible with the plane weave of the DLR-XT. However, the latter effect is not large and the predominant heat flux exploits transverse fibre thermal conductivity.

## 7. Conclusions

The finite element method has been used with multi-linear discretisations of tow longitudinal and transverse thermal conductivity data to predict composite response for two materials:

- (i) The finite element method employed has traceability to the thermo-mechanical properties of the constituent materials i.e. basic data for the fibres and matrices used in the tow model of Tang et al. (2009). Therefore the macroscopic unit cell properties have been predicted from properties that relate to the micro-scale.

- (ii) For the Nicalon-CAS  $0^\circ/90^\circ$  laminate, and a DLR-XT plain weave composite good agreement has been achieved with experimental data.
- (iii) For the Nicalon-CAS  $0^\circ/90^\circ$  laminate it is the wake debonding mechanism, modelled at the tow level by Tang et al. (2009), and incorporated in the tow data of Fig. 2, that is responsible for the degradation of transverse thermal conductivity.
- (iv) For the plain weave DLR-XT composite the degradation of transverse thermal conductivity is due to two mechanisms. For the initial strain range  $(\epsilon_{33})_\infty \leq 0.17\%$  it is the wake debonding mechanism, incorporated in the tow data of Fig. 3, that dominates; thereafter, the fibre/matrix interface air gaps are produced by a combination of shear strain  $\epsilon_{23}$  exceeding  $\epsilon_{23} = 0.1152\%$ , when the value of  $\sigma_{22}^\ell > \sigma_{22}^{\ell_0} = 3.5$  MPa, and by the tow wake debonding mechanism modelled by Tang et al. (2009).
- (v) For both the Nicalon-CAS and the DLR-XT materials it has been found necessary to include waviness in the finite element models to accurately model the unit cell stress–strain response, and the composite transverse thermal conductivity–strain response. For both materials a waviness angle of  $\xi = \pm 7^\circ$  has been used.
- (vi) The model for Nicalon-CAS does not invoke degradation of thermal properties by out-of-plane shear failure, but that for DLR-XT does.

## Acknowledgement

The authors gratefully acknowledge financial support from the EPSRC of Great Britain under Grant No: EP/D056276/1.

## Appendix A

### A.1. Mechanical and thermal response of a uni-directional tow

#### A.1.1. Tow stress–strain response

It is assumed that the stress–strain behaviour of a uni-directional tow, Fig. A1(a) is determined by a single-state damage variable,  $\omega$ , where  $\omega$  is the ratio of number of failed to the total number of fibres. If there is no fibre failure then  $\omega = 0$ , while  $\omega = 1$  represents complete failure of fibres (Tang et al., 2009). Fibre failure is determined by a Weibull (1939) statistical distribution, which correlates the damage variable,  $\omega$ , and the local composite stress,  $\sigma_{33}^\ell$ , by using two Weibull parameters: average fibre failure stress,  $\sigma_{ff}$ , and the Weibull index,  $m$ . The total stress on the fibres, given by Hayhurst et al. (1991), involves contributions from both the unfailed fibres, the first term on the right hand side, and from the frictional pull-out force that acts around the failed fibres, the last term on the right hand side:

$$\Sigma_0 = \frac{\sigma_0}{\sigma_{ff}} = \frac{\Sigma_{33}^\ell}{V_f} = \Sigma_f (1 - \omega)^A = (1 - \omega)^A \left[ -\left(\frac{\ell_0}{\ell}\right) \ln(1 - \omega) \right]^{\frac{1}{m}} + \frac{S[(1 - \omega)^D - (1 - \omega)]}{1 - D}. \quad (A1)$$

Differentiation of Eq. (A1) with respect to  $\omega$  gives:

$$d\omega/d\Sigma_{33}^\ell = (1/\alpha)[(1 - \omega)^{(A-1)}[(1/m)(-\ln(1 - \omega))^{(1-m)/m} - A(-\ln(1 - \omega))^{1/m}] + S(1 - D)^{-1}(1 - D(1 - \omega)^{(D-1)})^{-1}], \quad (A2)$$

where  $\alpha (=V_f)$  is the fibre volume fraction. The variation of the damage variable,  $\omega$ , with local tow strain,  $\epsilon_{33}^\ell$ , is given by Eq. (2) of Hayhurst et al. (1991) and also by Eq. (2.2) of Tang et al. (2009):

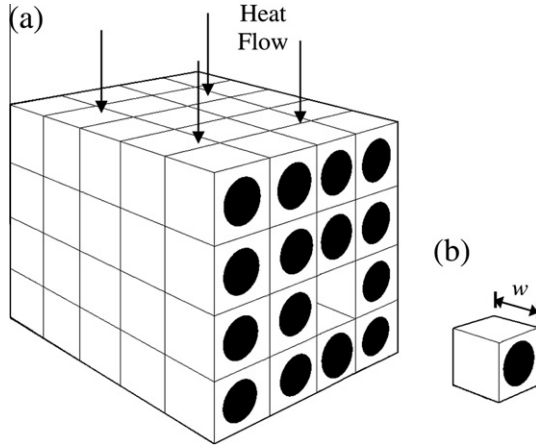


**Fig. A1.** (a) Schematic representation of the division of the composite tow into blocks of length equal to the matrix crack spacing  $w$  and fibres denoted by solid ellipses; and (b) representation of a single conducting block.

$$\frac{d\lambda_{33}^{\ell}}{d\Sigma_{33}^{\ell}} = \frac{\partial \lambda_{33}^{\ell}}{\partial \Sigma_{33}^{\ell}} + V_f \frac{\partial \lambda_{33}^{\ell}}{\partial E(\omega)} \frac{dE(\omega)}{d\omega} \frac{d\omega}{d\Sigma_{33}^{\ell}}, \quad (\text{A3})$$

where  $\lambda_{33}^{\ell} = \varepsilon_{33}^{\ell}/\varepsilon_{ff}$ ;  $\Sigma_{33}^{\ell} = \sigma_{33}^{\ell}/\sigma_{ff}$ ;  $\varepsilon_{ff}$  is the average fibre failure strain,  $\varepsilon_{ff} = \sigma_{ff}/E_f$ ;  $E_f$  is the initial Young's modulus of the entire composite and is given by  $E_f = V_f E_f + V_m E_m$ ;  $V_m$  is the volume fraction of the matrix;  $E_f$  and  $E_m$  are Young's moduli of fibre and matrix. Substitution of the Eq. (A3) into Eq. (A2) yields the relationship between the remote composite stress,  $\sigma_{\infty}$ , and the remote strain,  $\sigma_{33}^{\ell}$ , c.f. Hayhurst et al. (1991) and Tang et al. (2009):

$$\frac{d\lambda_{33}^{\ell}}{d\Sigma_{33}^{\ell}} = \frac{d(\varepsilon_{33}^{\ell}/\varepsilon_{ff})}{d(\sigma_{33}^{\ell}/\sigma_{ff})} = [(\ell_0/\ell)^{1/m} (1-\omega)^{A-1} [-(1/m) \ln(1-\omega)]^{1-m} - A[-\ln(1-\omega)]^{1/m} + \{S[(1-\omega)^D - (1-\omega)]/(1-D)\} \frac{(\sigma_0/\sigma_{ff})B}{\Theta(1-\omega)^{B+1}} + \frac{1}{\Theta(1-\omega)^B}], \quad (\text{A4})$$

where  $\sigma_0$  is the nominal fibre stress, given by Eq. (A1);  $A$ ,  $B$ ,  $D$  and  $S$  are material parameters, details of calibrating  $A$ ,  $B$ ,  $D$  and  $S$  are given by Tang et al. (2009);  $\Theta = (E_f + \Delta E_f)/E_f$  is a parameter related to the change of Young's modulus due to matrix cracking at  $\sigma_{mc}$ ; and,  $\ell$  and  $\ell_0$  are physical and reference lengths, respectively.

Eq. (A4) shows that the variation of the normalised stress with strain is a function of  $\omega$ . Eq. (A2) together with Eq. (A4) have been numerically integrated with respect to the damage variable  $\omega$  using the first order Euler method. The initial conditions are  $\omega = 0$ ,  $\sigma_{33}^{\ell}/\sigma_{ff} = 0$  and the final conditions is  $\omega = 1$ , when all fibres have failed. The time step for  $\omega$  has been carefully selected to be small enough to ensure the results have converged, and the curve accurately models all points close to the peak level. Substitution of the constituent material properties, given in table 1 of Tang and Hayhurst (in press) for Nicalon CAS, and in table A1 of Tang et al. (in press) for DLR-XT, into Eqs. (A2) and (A4), and following un-normalisation of  $\Sigma_{33}^{\ell}$  and  $\lambda_{33}^{\ell}$  in Eq. (A4) yields the stress-strain response for the uni-directional tow.

#### A1.2. Tow thermal behaviour

##### (i) Tow longitudinal thermal conductivity

Micrographs (Del Puglia et al., 2004b) show that the outer matrix of the DLR-XT composite undergoes cracking in manufacture, this occurs on planes perpendicular to the tow axis. The consequence of matrix cracking is to create a thermal barrier across the cracks and thus prevent heat flow through the matrix, hence the thermal

conductivity of the outer matrix parallel to the tow axis becomes zero during manufacture. The initial longitudinal thermal conductivity of the tow  $k_{\text{Tow-L}}^{\text{Initial}}$  is given by:

$$k_{\text{Tow-L}}^{\text{Initial}} = k_f V_f + k_{im} V_{im} + k_{om} V_{om} + k_{air} V_{air} \quad (\text{A5})$$

where  $k_{ff}$  is the longitudinal thermal conductivity of the fibres,  $k_{im}$  is the thermal conductivity if the inner matrix {amorphous carbon in the case of DLR-XT},  $k_{om}$  is the thermal conductivity if the outer matrix {zero, due to cracking of the SiC in the case of DLR-XT}, and  $k_{air}$  is the thermal conductivity of the air contained within the relevant porosity. The degradation of normalised longitudinal thermal conductivity,  $k_{\text{Tow-L}}^{\ell}/k_{\text{Tow-L}}^{\text{Initial}}$ , with damage  $\omega$ , both before and after matrix cracking are given, respectively by Eqs. (A.6) and (A.7) c.f. Tang et al. (2009):

$$\frac{k_{\text{Long}}^{\ell}}{k_{\text{Long}}^{\ell-\text{Initial}}} = \frac{k_{\text{Tow-L}}^{\ell}}{k_{\text{Tow-L}}^{\text{Initial}}} = \frac{k_{ff}/V_f(1-\omega) + k_{im}V_{im}}{k_{ff}/V_f + k_{im}V_{im} + k_{air}V_{air}}, \quad (\text{A6})$$

$$\frac{k_{\text{Long}}^{\ell}}{k_{\text{Long}}^{\ell-\text{Initial}}} = \frac{k_{\text{Tow-L}}^{\ell}}{k_{\text{Tow-L}}^{\text{Initial}}} = \frac{k_{ff}/V_f(1-\omega)}{k_{ff}/V_f + k_{im}V_{im} + k_{air}V_{air}}, \quad (\text{A7})$$

where the superscript  $\ell$  denotes local tow conditions,  $k_{ff}$  is the longitudinal thermal conductivity of fibres;  $V_{im}$  and  $k_{im}$  are the volume fraction and thermal conductivity of the inner matrix; and  $k_{air}$  and  $V_{air}$  are the thermal conductivity and volume fraction of air. The initial thermal conductivity  $k_{\text{Tow-L}}^{\text{Initial}}$  has been determined from equation (3.1) of Tang et al. (2009) using the properties listed in table 2 of Tang and Hayhurst (in press) for the Nicalon CAS material, and in tables A1 and A2 of Tang et al. (in press) for the DLR-XT material. Both Eqs. (A6) and (A7) show that the longitudinal thermal conductivity is a function of the damage variable  $\omega$ . Integration of Eqs. (A2) and (A4), and using Eq. (A1) for  $\sigma_{\infty}$ , yields the relationship between the composite strain,  $\varepsilon_{33}^{\ell}$ , and the damage variable,  $\omega$ . Substitution of  $\varepsilon_{33}^{\ell}$  for  $\omega$  in Eqs. (A6) and (A7), and substitution of the material properties yields the predicted degradation of normalised longitudinal thermal conductivity with composite strain,  $\varepsilon_{\infty}$ .

Eq. (A7) predicts that after matrix cracking, longitudinal thermal conductivity is determined by the fraction  $(1-\omega)$  of unfailed fibres. Therefore, before the majority of fibres begin to fail, both materials show little degradation.

##### (ii) Tow Transverse thermal conductivity

###### (a) Initial transverse thermal conductivity

Prediction of the transverse thermal properties of a uni-directional tow in its undamaged state is more complex than in the longitudinal direction. The initial transverse thermal conductivity,  $k_{\text{Tow-T}}^{\text{Initial}}$ , can be calculated using Eq. (3.3) of Tang et al. (2009):

$$(1 - V_f)(k_{f\perp} - k_{im}) = (k_{f\perp} - k_{\text{Tow-T}}^{\text{Initial}}) \left( k_{im}/k_{\text{Tow-T}}^{\text{Initial}} \right)^{1/X+1}, \quad (\text{A8})$$

where  $k_{f\perp}$  is the transverse thermal conductivity for the fibre or discontinuous phase;  $k_{im}$  is the thermal conductivity for the continuous phase or inner matrix; and the parameter  $X$  is a shape factor for the discontinuous phase.

The development of Eq. (A8) has been formalised by Whittaker and Taylor (1990). Eq. (A8) describes transverse heat conduction through a two-phase medium: the matrix material is treated as a continuous phase and the cylindrical fibres as a discontinuous phase. The shape factor  $X = 1$  relates to a regular array of cylindrical fibres (Whittaker and Taylor, 1990). Rearrangement of Eq. (A8) gives  $k_{\text{Tow-T}}^{\text{Initial}}$  in terms of  $k_{im}$ ,  $k_{f\perp}$  and  $V_f$ :

$$k_{\text{Tow-T}}^{\text{Initial}} = (1/2k_{im})[\alpha \pm \sqrt{\alpha^2 - 4k_{f\perp}^2 k_{im}^2}], \quad (\text{A9})$$

where  $\alpha = (k_{f\perp}^2 + k_{im}^2)(1 - V_f)^2 + 2k_{f\perp}k_{im}V_f(2 - V_f)$ .



For the Nicalon-CAS material,  $k_{Tow-T}^{Initial}$  is the transverse thermal conductivity of the entire tow, and substitution of material data from Table 2 of Tang and Hayhurst (in press) yields the initial transverse thermal conductivity.

However, for the DLR-XT material, the term  $k_{Tow-T}^{Initial}$  in Eq. (A9) is associated with the central inner tow only (c.f. Fig. 9 of Tang et al., 2009) and is designated as  $k_{TB,Cent.}^{Initial}$ . In addition to the inner tow region, the SiC outer matrix has to be considered. In developing their one-dimensional transverse heat flow model, Tang et al. (2009) split the tow cross-section into two zones A and B. Zone A comprises two layers of the SiC outer matrix having a length equal to that of the heat flow path; and, zone B comprises the central fibre/inner matrix region sandwiched between two outer layers of SiC. This is illustrated in Fig. 9 of the paper by Tang et al. (2009). The transverse thermal conductivity through cross-sections B,  $k_{TB}$ , was determined using  $k_{TB,Cent.}^{Initial}$ , from Eq. (A9), and  $k_{TA}$  of the outer SiC matrix. The total heat flux through cross-sections A and B was formulated using a one-dimensional parallel (A + B) - serial (B) heat flow model which leads to the overall transverse thermal conductivity of regions A plus B:

$$k_T = k_{TA}V_A + k_{TB}V_B \quad (A10)$$

where  $V_A$  and  $V_B$  are the volume fractions of zones A and B.

(b) *Degradation of tow transverse thermal conductivity with strain due to matrix cracking and wake debonding.*

A uni-directional tow, Fig. A1(a), can be divided into many identical blocks of a length equal to the matrix crack spacing,  $w$ , as shown in Fig. A1(b). Once the wake debonding failure criteria, c.f. Tang et al. (2009), has been satisfied within a block, the interfacial failure introduces a circumferential air gap that surrounds the fibre, and it is this cylindrical air gap which impedes the heat flow transverse to this block c.f. Fig. 2. To evaluate the effect of the cylindrical air gap on the transverse thermal conductivity, Eq. (A8) has been used again. The fibre-matrix combination is homogenised and treated as a continuous phase with a constant transverse thermal conductivity of  $k_{Tow-T}^{Initial}$  and the air gap is treated as a discontinuous phase that varies with volume,  $V_p$  given by:

$$V_p = \frac{N\pi(D_f d + d^2)}{\varphi(b - 2t_{om})(c - 2t_{om}) + N\pi(D_f d + d^2)}, \quad (A11)$$

which varies with the number of wake debonded blocks,  $N$ , within the region shown schematically in Fig. A1(a); where  $b$  and  $c$  are the width and height of the tow;  $t_{om}$  is the thickness of the outer matrix;  $d$  is the average thickness of the air gap produced by wake debonding, and  $\varphi$  is the number of matrix crack spacings. Eq. (A11) has been derived as equation (3.12) in Tang et al. (2009).

In Eq. (A8),  $k_{Tow-T}^{Initial}$  is replaced by  $k_{Tow-T}$ ;  $k_{f,l}$  is replaced by  $k_{air} = 0$ ;  $k_{im}$  is replaced by  $k_{Tow-T}^{Initial}$ ; and  $V_f$  is replaced by  $V_p$ ; hence:

$$k_{Tow-T} = k_{Tow-T}^{Initial}(1 - V_p)^{(X+1)/X}, \quad (A12)$$

where the shape factor  $X$  relates the shielding effects of wake debonded cracks to the transverse thermal conductivity. The value  $X = 0.1$  is the shape factor for this type of crack (Whittaker and Taylor, 1990).

A model, based upon the maximum interfacial shear stress, has been developed to calculate the number of blocks,  $N$ , that have wake debonded out of a total of  $N_T$  within the tow. After matrix cracking, fibres carry the majority of the load; however, before wake debonding occurs, a small amount of the load is transferred to the matrix via the interfacial shear stress. Therefore, as the load in the fibres increases so does the shear stress until a critical value is reached at the location of the matrix crack, and wake debonding takes place. It is therefore important to be able to calculate the

maximum shear stress along the fibre-matrix interface at different levels of strain. An equation for the shear stress at the matrix crack,  $\tau(x = 0)$ , in a particular block before the inception of wake debonding, for different levels of composite strain, is given by Eq. (3.13) of Tang et al. (2009) as:

$$\tau(x = 0) = \frac{((\sigma_{33}^f/E_f V_f(1 - \omega)) - (\epsilon_{33}^f \sigma_{ff}^f/\epsilon_{ff} E_l))E_f A_f \beta^2 w}{\pi D_f (\beta w \tanh^{-1}[\beta w/2] - 1)}, \quad (A13)$$

where  $\beta = (2\pi G_f/(E_{im} A_f \ln(2R_b/D_f)))^{1/2}$ ;  $2R_b$  is the height of a block;  $G_f$  is the shear modulus of fibre;  $A_f$  is the cross-sectional area of a fibre; and  $E_l$  is the initial overall Young's modulus of the composite.

The shear failure stress of each individual block is assumed to be determined by a Weibull distribution (Tang et al., 2009), and it is described by two parameters: the average interfacial shear stress,  $\tau_c$ , and the Weibull index,  $g$ , and it can be expressed by:

$$N/N_T = 1 - [\exp\{-(\tau/\tau_c)^g\}]. \quad (A14)$$

Substitution of Eqs. A10, A11, A13 and A14 into Eq. (A12) yields the variation of the transverse thermal conductivity with composite strain for a uni-directional tow:

$$\frac{k_{Trans}^f}{k_{Trans}^{f-Initial}} = \frac{k_{Tow-T}}{k_{Tow-T}^{Initial}} = \left[ 1 - \left( \Phi \left[ 1 - \exp \left\{ - \left[ \left( \frac{\sigma_{\infty}}{E_f V_f (1 - \omega)} - \frac{(\epsilon_{\infty}/\epsilon_{ff}) \sigma_{ff}^f}{E_l} \right) \Psi \right]^g \right\} \right]^{-1} + 1 \right)^{-1} \right]^{\frac{(X+1)}{X}}, \quad (A15)$$

where the parameters  $\Psi$  and  $\Phi$  are given by  $\Psi = E_f A_f \beta^2 w / \tau_c \pi D_f (\beta w \tanh^{-1}[\beta w/2] - 1)$  and  $\Phi = bc/\eta \psi \pi (D_f d + d^2)$ . The values of the tow geometry parameters  $\eta$ ,  $\psi$ , are given in the Appendix of Tang and Hayhurst (in press) for Nicalon-CAS; and in tables A1 and A2 of Tang et al. (in press) for DLR-XT. Eq. (A15) is derived as equation (3.18) in Tang et al. (2009).

For the Nicalon-CAS material, the degradation of transverse thermal conductivity with composite strain can be calculated using Eq. (A15) and material data given in Tang and Hayhurst (in press).

For the DLR-XT material, Eq. (A15) gives the degradation of thermal conductivity of the central or inner region of zone B, with  $k_{TB,Cent.}/k_{TB,Cent.}^{Initial} = k_{Tow-T}/k_{Tow-T}^{Initial}$ , c.f. Fig. 9 of Tang et al. (2009). For the entire tow, the effect of the outer SiC matrix must be considered. As outlined earlier, micrographs by Del Puglia et al. (2004) show that the outer matrix of the DLR-XT undergoes cracking in manufacture. Since these cracks, which have negligible width, are predominantly located in planes perpendicular to the longitudinal tow axis, and in turn are coincident with the heat flow direction, the thermal conductivity of the SiC matrix does not degrade with uni-axial strain (Del Puglia et al., 2005).

To consider the effect of the intact outer SiC matrix, parallel and serial rule of mixtures equations must be applied to the cross-sectional zones A and B. This yields an equation for the overall degradation of normalised transverse thermal conductivity for the DLR-XT tow material, derived as Eq. (3.11) of Tang et al. (in press):

$$\frac{k_{Trans}^f}{k_{Trans}^{f-Initial}} = \frac{k_{Tow-T}}{k_{Tow-T}^{Initial}} = \frac{k_{TA}V_A}{k_{Tow-T}^{Initial}} + \frac{k_{om}\tilde{V}_B V_B}{k_{Tow-T}^{Initial}\tilde{V}_{B,Cent.}} \left/ \left[ \frac{\tilde{V}_{om}^B}{\tilde{V}_{B,Cent.}} + \left\{ \frac{k_{TB,Cent.}^{Initial}}{k_{om}} \bullet \left[ 1 - \left( \Phi \left[ 1 - \exp \left\{ - \left[ \left( \frac{\sigma_{\infty}}{E_f V_f (1 - \omega)} - \frac{(\epsilon_{\infty}/\epsilon_{ff}) \sigma_{ff}^f}{E_l} \right) \Psi \right]^g \right\} \right]^{-1} + 1 \right)^{-1} \right]^{\frac{(X+1)}{X}} \right]^{-1} \right] \right. \right. \quad (A16)$$

where  $V_A$  and  $V_B$  are respectively the volume fractions of zones A and B;  $\tilde{V}_B$  is the volume of zone B;  $\tilde{V}_{om}^B$  and  $\tilde{V}_{B,Cent.}^B$  are the respective volumes of outer matrix and inner tow within zone B;  $k_{TA}$  and  $k_{om}$  are the respective thermal conductivities of zone A and the outer matrix.

Use of Eq. (A16) and the material properties, given in tables A1 and A2 of Tang et al. (in press) for the DLR-XT material, yields the degradation of transverse thermal conductivity with strain for a uni-directional tow of DLR-XT.

When calculating the degradation of transverse thermal conductivity from Eq. (A15) for the Nicalon-CAS material and from Eq. (A16) for DLR-XT, it is necessary to evaluate  $\sigma_{33}^d$  as a function of  $\epsilon_{33}^d$  using Eq. (A4). In this equation, the common thread between  $\sigma_{33}^d$  and  $\epsilon_{33}^d$  is the damage variable,  $\omega$ . Integration of Eq. (A4), with respect to  $\omega$ , for the  $\epsilon_{33}^d - \omega$  variation, together with Eq. (A2) for the  $\sigma_{33}^d - \omega$  variation, as outlined earlier, yields the variation of  $\sigma_{33}^d$  with  $\epsilon_{33}^d$ .

### A.1.3. Variation of normalised number of wake debonded blocks $N/N_T$ with composite strain $(\epsilon_{33})_\infty$ ; and catastrophic failure strain $\epsilon_{wd}$ due to instantaneous pullout deactivation

(i) Number of wake debonded blocks  $N/N_T$  with composite strain  $(\epsilon_{33})_\infty$  Shown in Fig. A2(a) is the stress–strain curve for a DLR-XT tow predicted from the materials properties of the composite constituent materials, using Eqs. (A2) and (A4). Superimposed in the same figure is the curve of the normalised number of failed blocks  $N/N_T$  within the tow. The latter has been determined from Eqs. (A13) and (A14), using Eqs. (A2) and (A4) for the tow stress–strain. The figure shows a dramatic rise in  $N/N_T$  over a narrow range of strain at approximately  $N/N_T = 0.5$ .

(ii) Dynamic fibre failure strain  $\epsilon_{wd}$  due to instantaneous pullout deactivation.

Blacklock and Hayhurst (2009, in press) reported the initial elastic properties and multi-axial failure of CMC fibre tows. The

initial elastic properties were predicted based on a micromechanical finite element analysis of representative volume elements from the constituent properties of fibres and matrices. Blacklock and Hayhurst (in press) proposed that the tensile stress,  $(\sigma_{22})$ , transverse to the tow c.f. Fig. 5, induced by the composite lay-up has the effect of facilitating the initiation of wake debonding, which then negates the stress contribution from fibre pullout process; and, they assumed that the average wake debonding strain,  $\epsilon_{wd}$ , be defined as the strain at which half of all blocks, shown in Fig. A1(a), have wake debonded i.e.  $N/N_T = 0.5$ . It was also argued that by virtue of the way in which a ductile CMC is designed, the average wake debonding strain,  $\epsilon_{wd}$ , is slightly less than the peak composite strain, and hence at this point the fibres are stressed to a high fraction of the average fibre failure stress. The effect of approximately one half of all blocks in the tow simultaneously undergoing: wake debonding; propagation of a fibre tensile stress wave; and, subsequent doubling of the tensile wave by reflection on the centre line of each block, shown in Fig. A1; causes catastrophic multiple failure of all fibres. If this theory is used for the DLR-XT material, then the predictions shown in Fig. A2 are obtained.

## References

- Argyris, J., Tenek, L., Oberg, F., 1995. A multilayer composite triangular element for steady-state conduction/convection/radiation heat transfer in complex shells. *Comput. Meth. Appl. Mech. Eng.* 120, 271–301.
- Blacklock, M., Hayhurst, D.R., 2009. Initial elastic properties of ceramic matrix composite fibre tows. Research report No. DMM. 09.07, School of Mechanical, Aerospace and Civil Engineering, The University of Manchester, UK.
- Blacklock, M., Hayhurst, D.R., in press. Multi-axial failure of ceramic matrix composite fibre tows. *J. Appl. Mech.*
- Del Puglia, P., Sheikh, M.A., Hayhurst, D.R., 2004a. Classification and quantification of initial porosity in a CMC laminate. *Compos. Part A: Appl. Sci. Manuf.* 35, 223–230.
- Del Puglia, P., Sheikh, M.A., Hayhurst, D.R., 2004b. Modelling the degradation of thermal transport in a CMC material due to three difference classes of porosity. *Model. Simul. Mater. Sci. Eng.* 12, 357–372.
- Del Puglia, P., Sheikh, M.A., Hayhurst, D.R., 2005. Thermal transport property prediction of a CMC laminate from base material properties and manufacturing porosities. *Proc. R. Soc. A* 461, 3575–3597.
- Evans, A.G., Naslain, R., 1995. High-temperature ceramic-matrix composites. *Ceram. Trans.* 57, 381–388.
- Fourier, J., 1822. *Theorie Analytique de la Chaleur*. Firmin Didot. ISBN 9781108001809 (reissued by Cambridge University Press, 2009).
- Harris, B., Habib, F.A., Cooke, R.G., 1992. Matrix cracking and the mechanical behaviour of SiC-CAS composites. *Proc. R. Soc. A* 437, 109–131.
- Hayhurst, D.R., Leckie, F.A., Evans, A., 1991. Component design-based model for deformation and rupture of tough fibre-reinforced ceramic matrix composites. *Proc. R. Soc. Lond. A* 434, 369–381.
- Klett, J.W., Ervin, V.J., Edie, D.D., 1999. Finite-element modelling of heat transfer in carbon/carbon composites. *Compos. Sci. Technol.* 59, 593–607.
- Lu, T.J., Hutchinson, J.W., 1996. Effect of matrix cracking on the overall thermal conductivity of fibre-reinforced composites. In: Cahn, R.W., Evans, A.G., McClean, M. (Eds.), *High-temperature Structural Materials*. Chapman and Hall, London, UK, pp. 177–192.
- Marshall, D.B., Cox, B.N., 2008. Integral textile ceramic structures. *Annu. Rev. Mater. Res.* 38, 425–443.
- McGlockton, M.A., Cox, B.N., McMeeking, R.M., 2003. A binary model of textile composites. III: high failure strain and work of fracture in 3D weaves. *Acta Metall. Mater.* 51, 1573–1600.
- Sheikh, M.A., Taylor, S.C., Hayhurst, D.R., Taylor, R., 2001. Microstructural finite element modelling of a ceramic matrix composite to predict experimental measurements of its macro thermal properties. *Model. Simul. Mater. Sci. Eng.* 9, 7–23.
- Sheikh, M.A., Taylor, S.C., Hayhurst, D.R., Taylor, R., 2009. Experimental investigation of the effect of mechanical loading on thermal transport in ceramic matrix composites. *J. Multiscale Model.* 1 (3–4), 403–431.
- SIMULIA, 2006 ABAQUS user's manual. Version 6.6. Providence, Rhode Island, US.
- Tang, C., Blacklock, M., Hayhurst, D.R., 2009. Uni-axial stress–strain response and thermal conductivity degradation of ceramic matrix composite fibre tows. *Proc. R. Soc. A* 465, 2849–2876.
- Tang, C., Blacklock, M., Hayhurst, D.R., in press. Stress–strain response and thermal conductivity degradation of ceramic matrix composite fibre tows in 0–90° uni-directional and woven composites. *J. Compos. Mater.*
- Tang, C., Hayhurst, D.R., in press. Predictions of thermo-mechanical behaviour of a Nicalon-CAS 0–90° ceramic matrix composite from constituent materials properties. *J. Compos. Mater.*
- Weibull, W., 1939. A statistical theory of strength of materials. In: *Proceedings of Royal Swedish Institute*, Stockholm, p. 151.

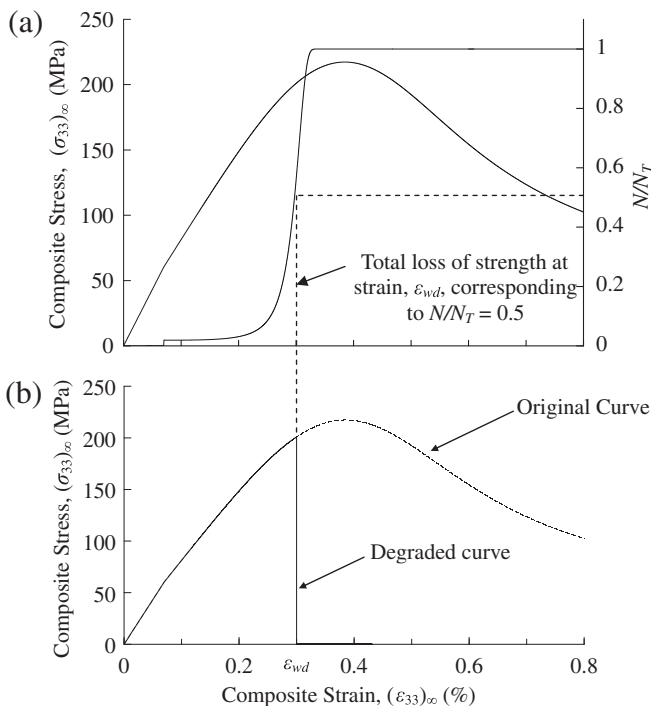


**Fig. A2.** Material properties for a CMC composite: (a) stress–strain curve of a uni-directional tow under longitudinal loading and variation of normalised number of wake debonded blocks  $N/N_T$  with composite strain  $(\epsilon_{33})_\infty$ ; and (b) stress–strain curve of a uni-directional tow (Blacklock and Hayhurst, in press).

- Whittaker, A.J., Taylor, R., 1990. Thermal transport properties of carbon-carbon fibre composites. III: Mathematical modelling. *Proc. R. Soc. A* 430 (1878), 199–211.
- White, J.L.e., Knutsson, A., 1982. Theory of thermal conductivity, heat conduction and convective heat transfer in fiber filled polymer composites. *Polymer Eng. Rev.* 2 (1), 71–82.
- Yang, Q., Cox, B., 2003. Spatially averaged local strain in textile composites via the binary model formulation. *J. Eng. Mater. Technol. Trans. ASME* 125, 418–425.
- Zhang, D., Hayhurst, D.R., 2010. Stress-strain and fracture behaviour of 0/90 and plain weave ceramic matrix composites from tow multi-axial properties. *Int. J. Solids Struct.* 47 (21), 2958–2969. doi:[10.1016/j.ijsolstr.2010.06.023](https://doi.org/10.1016/j.ijsolstr.2010.06.023).